Supplement of The Cryosphere, 15, 3279–3291, 2021
https://doi.org/10.5194/tc-15-3279-2021-supplement

The Cryosphere
Open Access

Supplement of

Geophysical constraints on the properties of a subglacial lake in northwest Greenland

Ross Maguire et al.

Correspondence to: Ross Maguire (rmaguire@umd.edu)

S1. Seismic and radar velocity structure

Estimates of lake depth using travel times of seismic or radar reflections depend on knowing the velocity of the medium through which the waves travel. In order to reliably compare depth estimates from each technique, it is important to determine a self-consistent model of the structure and material properties of the ice sheet from top to bottom. In this study, the average seismic velocity structure of the ice sheet was determined using a normal moveout velocity analysis of the primary lake top reflection, which yielded a velocity of V_P = 3700 +/- 40 m s^{-1}. Since this value averages the entire ice column consisting of both firn and glacial ice, it is lower than most values reported for glacial ice, which typically range between 3750 – 4000 m s^{-1} (e.g, Gusmeroli et al., 2012). Because radar velocity varies significantly between ice and firn, accurate lake depth determination with GPR requires knowing the depth and properties of both the firn and underlying glacial ice. Here, we estimate the firn depth and material properties using a seismic refraction survey. For each shot gather, we measured the P wave travel time at all geophones (Fig. S1) and inverted for a best fitting shallow velocity structure using the software REFRACT (Burger et al., 2006). Given the maximum source receiver offset of 230 m, the velocity model is limited in depth resolution to approximately 50 m. At the lower bound of the refraction profile V_P is approximately 2850 m s^{-1}, indicating that the firn layer extends deeper than the resolution of the survey (Fig. S2a). However, given an average velocity within the ice sheet of 3700 m s^{-1}, we can place constraints on the depth of the firn by assuming a velocity in both the lower firn layer (i.e., the firn that lies below the depth of resolution) and the underlying glacial ice. This is illustrated in Fig. S2b, which shows how the estimated firn thickness trades off with the velocity of the lower firn layer and underlying glacial ice. In our preferred model, we assume the lower firn layer and underlying glacial ice to have velocities of V_P = 3000 m s^{-1} and V_P = 3800 m s^{-1}, respectively, which yields a firn thickness of 80 m. A thicker firn layer is possible if the velocity of either the lower firn layer or the underlying glacial ice is faster than our preferred model, although a thinner firn layer is unlikely since the ice sheet velocity below the firn would need to be unrealistically slow for glacial ice.

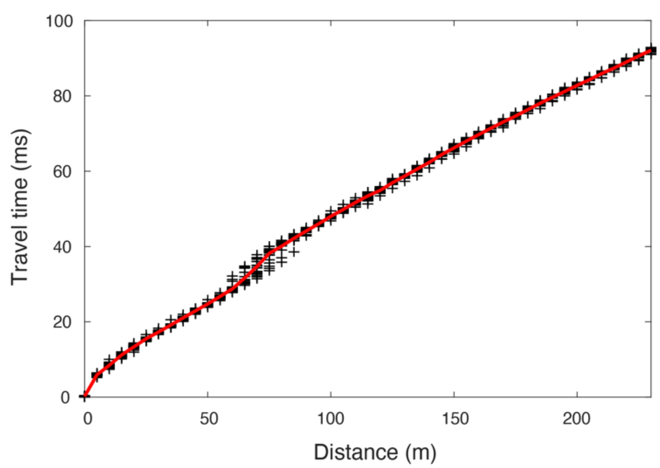

Figure S1. Results of seismic refraction survey. Scatter points indicate the measured P wave arrival time, and the red line shows the predicted travel times for the preferred model.

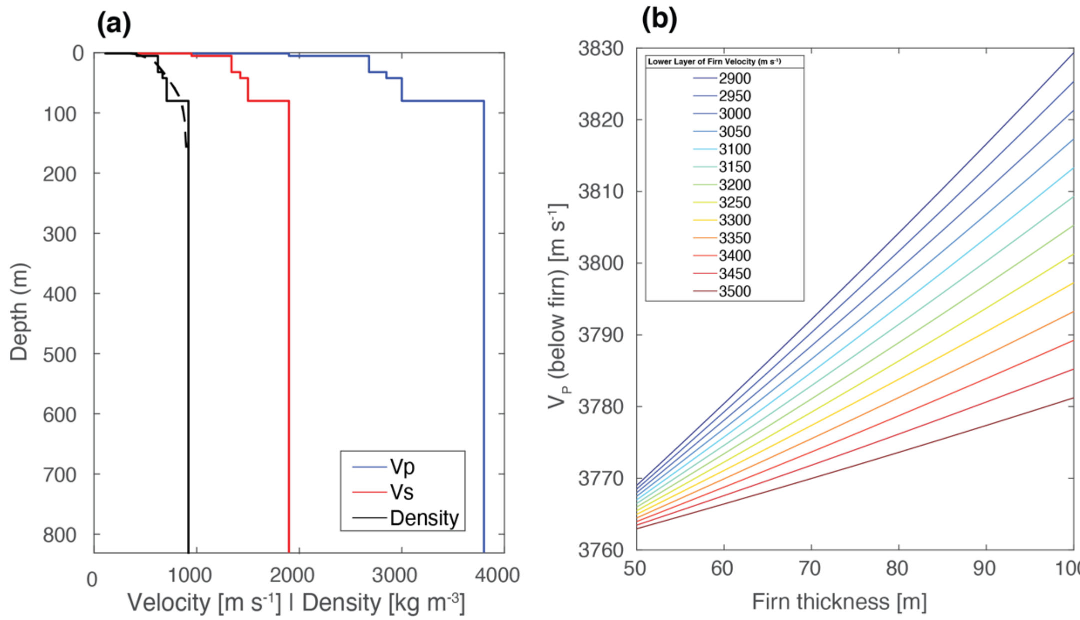

Figure S2. (a) Preferred seismic velocity and density structure, which includes an 80 m thick layer of firn overlying glacial ice with a V_P of 3800 m s^{-1}. Vs is assumed to be half of V_P, and density is determined using Equations S1 and S2. The dashed black line shows the density profile of the DYE-3 ice core (Gundestrup & Hansen, 1984) from southern Greenland. (b) Firn thickness analysis. Each line corresponds to an assumed firn velocity below 50 m. The velocity of the ice below the firn is calculated for total firn thicknesses ranging from 50 – 100 m, given the constraint of an average (RMS) velocity of 3700 m s^{-1} in the firn and ice column.

The density profile is scaled from V_P using a simple porosity model. First the porosity is determined using Equation S1, where φ is porosity, and $V_{P\,firn}$, $V_{P\,ice}$, and $V_{P\,air}$, are the P velocities of firn, glacial ice, and air respectively. Next, the density profile ρ(z) is determined with a two phase mixing model between ice and air, assuming that the density of ice ρ_{ice} is 950 kg m^{-3} and the density of air ρ_{air} is 1.22 kg m^{-3} (Equation S2).

$$\varphi = \frac{V_{P\,firn} - V_{P\,ice}}{V_{P\,air} - V_{P\,ice}}$$

Equation S1.

$$\rho(z) = (1 - \varphi)\rho_{ice} + \varphi\rho_{air}$$

Equation S2.

Lastly, to obtain radar velocity, use the scaling law of Kovacs *et al*., (1995):

$$V(z) = \frac{V_{air}}{[1 + 8.45x10^{-4}\,\rho(z)]}$$

Equation S3.

Where $V(z)$ is the radar velocity in m μs^{-1}, and V_{air} is the radar velocity in vacuum (300 m μs^{-1}). Figure S3 shows the scaled radar velocities in each layer of the seismic velocity model. The average radar velocity of the profile of 172 m μs^{-1} is used to convert radar two-way travel time to depth.

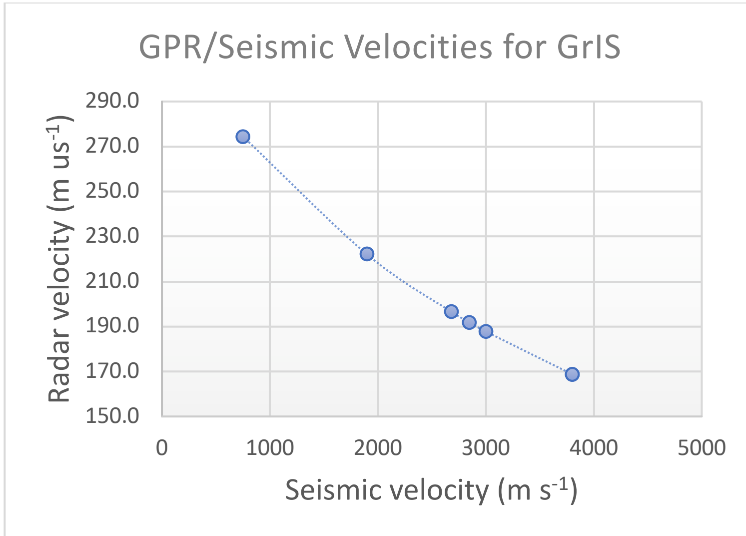

Figure S3. GPR velocities scaled from seismic velocities.

S2. Polarity analysis

If liquid water or soft dilatant sediment is present at the base of ice, the observed polarity of the primary bed reflection should be opposite to that of the seismic source (e.g., Muto et al., 2019). In Fig. S4 we show an example of our polarity analysis using data from shot gather 2 in our seismic line, which is located towards the western end of the survey, above the subglacial lake region (Fig. S4). As shown in Fig. S4b, we pick the first large positive peak of the direct arrival to define the source polarity. While the large positive peak of the direct arrival is preceded by a slight downswing, the amplitude of the downward pulse is much smaller than the positive peak, so we consider this as a sidelobe. The first large downswing of the R1 arrival is interpreted as the phase of the primary bed reflection (Fig. S4c). This negative pulse is followed by a positive pulse of roughly the same amplitude, which likely corresponds to the large negative downswing following the first peak of the direct arrival. Thus, the polarity analysis suggests that the bed is composed of a material with a lower acoustic impedance than glacial ice (e.g., water or dilatant till).

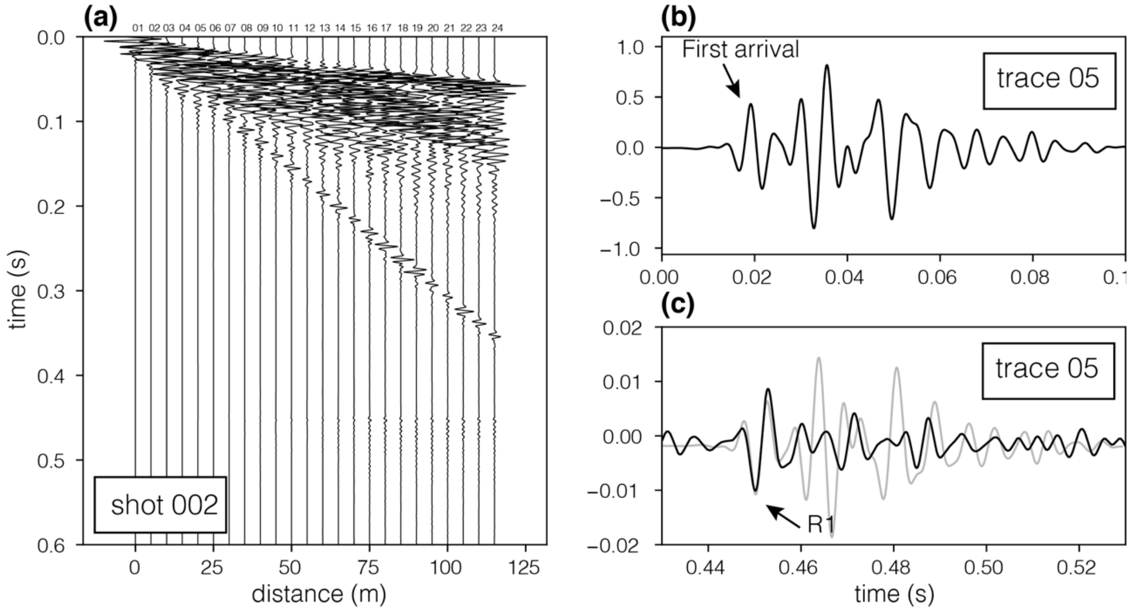

Figure S4: Reflection polarity analysis. Panel (a) shows a record section of shot gather 2 in our seismic survey, which is located above the subglacial lake. Close-up views of the first arrival and R1 reflection on a single trace are shown in panels (b) and (c), respectively. In (c), the grey line shows the waveform of the first arrival (i.e., the waveform shown in (b)) after being inverted, scaled, and aligned with the R1 reflection. All data is bandpass filtered between 100 – 250 Hz using a 2-corner zerophase Butterworth filter.

S3. Thermal modeling

In order to estimate the temperature in the ice above the lake, we use the steady state conservation of energy equation,

$$\rho c \frac{\partial T}{\partial t} = 0 = \frac{\partial}{\partial x_i} k_{ij} \frac{\partial T}{\partial x_j} - \rho c \dot{u}_k \cdot \frac{\partial T}{\partial x_k} - \dot{Q}$$

Equation S4.

where T is the temperature, ρ is density, c is the specific heat capacity, k is conductivity, and $\dot{u}$ is the velocity. Tensor indices i, j, k are defined as 1 and 2 being in the horizontal along and across flow directions and 3 as the vertical. The first, second, and third terms on the right-hand side represent heat diffusion, advection, and source terms, respectively. The sources are combined into $\dot{Q}$ and for this case they include both the geothermal flux and that due to latent heat of melting or freezing at the lake ice boundary: $\dot{Q}_{freeze} = -L\dot{m}$, where L is the latent heat for ice and $\dot{m}$ is the melt rate. Freezing of ice (negative $\dot{m}$) generates heat at the lake interface. In order to apply this to the ice over the lake, we make several simplifying assumptions:

1. We assume one dimensional geometry. For our low-sloping icefield, this is a reasonable assumption for several reasons. Considering a typical lapse rate of 7° K per kilometer, $\frac{\partial T}{x_1} \sim \frac{\partial T}{x_2} \ll \frac{\partial T}{x_3}$; therefore, even though we have a non-zero horizontal along-flow velocity, the effect of the advection of temperature from upstream is negligible compared to the vertical temperature gradient.

2. We assume that the vertical velocity linearly decreases from the surface (Cuffey & Paterson, 2010).

3. We assume that ice density is constant and equal to 920 kg m^{-3} . This assumption is weak for a compacting firn column, however our firn column is small compared to the full ice depth and we estimate an uncertainty due to this assumption of less than 0.1° C. We could however, estimate the effect of differing densities by varying the diffusivity (conductivity and specific heat).

4. We assume the conductivity (2.3 W m^{-1} K^{-1}) and specific heat (2000 J kg^{-1} K^{-1}) are uniform. This assumption results in an uncertainty of similarly less than 0.1° C.

5. We assume that the melt or freezing rates at the lake/ice boundary are small enough that the ice thickness is not changing significantly and we can assume steady state.

6. We assume that there is no convection or other currents within the lake and therefore that the bottom boundary condition is the heat flux at lake/ice boundary which is a combination of geothermal flux and melting or freezing. We vary the surface temperature, the geothermal flux, the freezing rate, and the surface vertical velocity (the accumulation rate in ice equivalent) over a range of values to test hypotheses for lake water temperature.

$$\frac{k}{\rho c}\frac{\partial^2 T}{\partial x_3^2} - \dot{u}_3\frac{\partial T}{\partial x_3} = \dot{Q}_{geo} + \dot{Q}_{freeze}$$

Equation S5.

We solve this using a control volume method (e.g., Patankar, 1980).

S4. Hydraulic head estimates

Water will flow down the hydraulic head gradient according to hydraulic potential theory. We use the theory from Shreve (1972) and similarly applied in Badgeley et al., (2017):

$$H = S + \left(\frac{\rho_w}{\rho_i}\right)B$$

Where S is the surface elevation, B is the bed elevation (Fig. S5a), ρ_w is the density of water (1000 kg m^{-3}) and ρ_i is the density of ice (we used 920 kg m^{-3}). We assume that basal water pressure equals overburden pressure (i.e. zero effective pressure).

The hydraulic head (H) is shown in Fig. S5b. Because the head is dominated by surface topography, the gradient in hydraulic head is downslope from the ice divide despite bedrock lows where the lake is located. Higher resolution bed topography might result in stronger subglacial connections; however, at this point the surface topography dominates the general subglacial pathways and would prevent water from flowing into the subglacial lake from the ice margins.

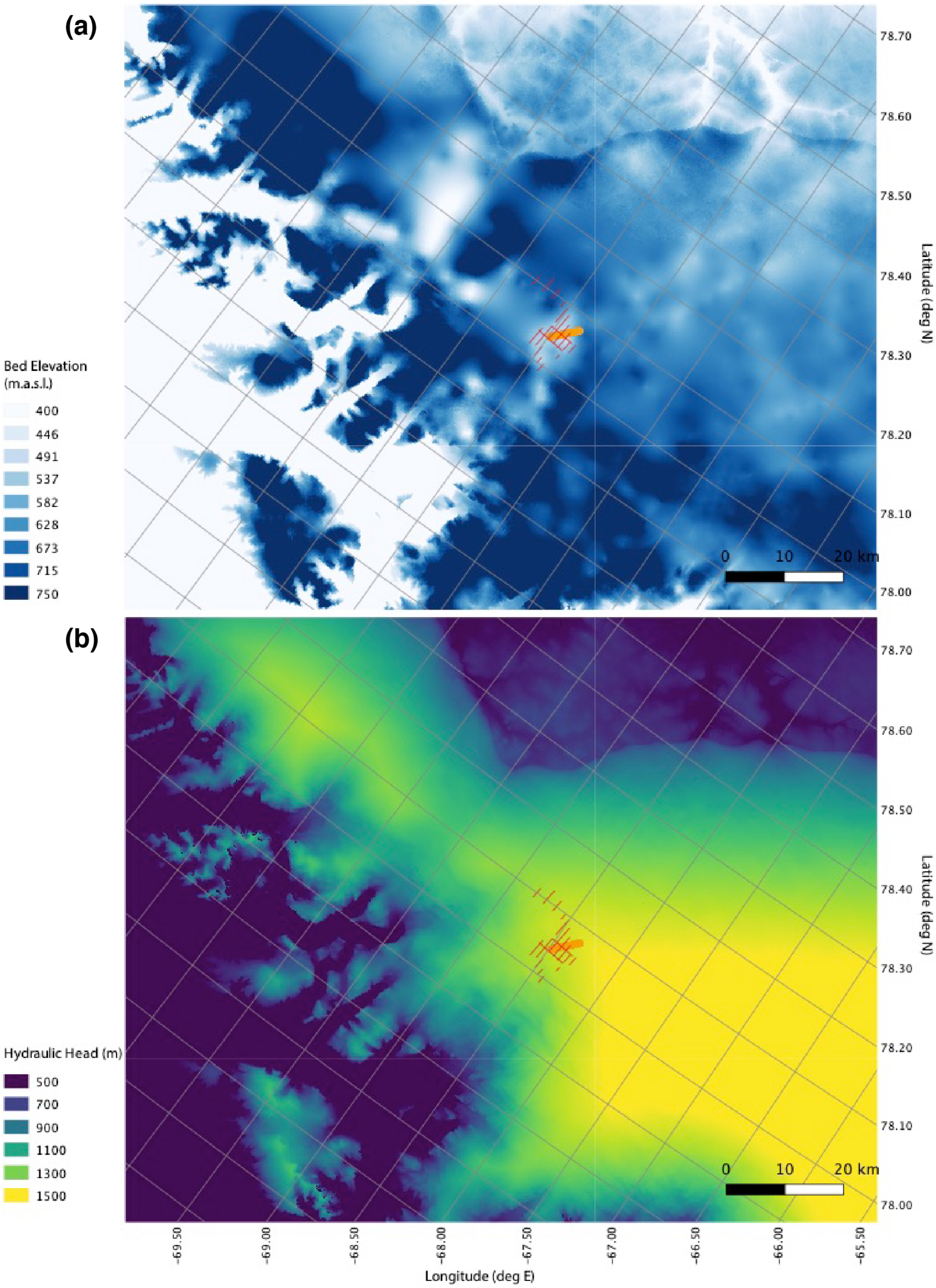

Figure S5: (a) Bed elevation from BedMachine v3 (Morlighem et al., 2017).The red lines show the area outlined as lake detection from Palmer *et al.* (2013). The orange dots are the radar profile we use in this study. (b) Hydraulic head calculated from the surface and bed elevations.

5. Seismic shot locations

shot #	lat (geophone 1)	lon (geophone 1)	offset (m)	total offset (m)	Line #	elevation (m)
1	78.05494	-68.43001	-115	0	Line1	1359
2	78.05494	-68.43001	0	0	Line1	1359
3	78.05494	-68.43001	115	0	Line1	1359
4	78.05494	-68.43001	230	0	Line1	1359
5	78.05635	-68.42283	-115	230	Line2	1355
6	78.05635	-68.42283	0	230	Line2	1355
7	78.05635	-68.42283	115	230	Line2	1355
8	78.05635	-68.42283	230	230	Line2	1355
9	78.05787	-68.41564	-115	460	Line3	1360
10	78.05787	-68.41564	0	460	Line3	1360
11	78.05787	-68.41564	115	460	Line3	1360
12	78.05787	-68.41564	230	460	Line3	1360
13	78.05908	-68.40867	-115	690	Line4	1357
14	78.05908	-68.40867	0	690	Line4	1357
15	78.05908	-68.40867	115	690	Line4	1357
16	78.05908	-68.40867	230	690	Line4	1357
17	78.06075	-68.40117	-115	920	Line5	1355
18	78.06075	-68.40117	0	920	Line5	1355
19	78.06075	-68.40117	115	920	Line5	1355
20	78.06075	-68.40117	230	920	Line5	1355
21	78.06218	-68.39438	-115	1150	Line6	1351
22	78.06218	-68.39438	0	1150	Line6	1351
23	78.06218	-68.39438	115	1150	Line6	1351
24	78.06218	-68.39438	230	1150	Line6	1351
25	78.0636	-68.38708	-115	1380	Line7	1365
26	78.0636	-68.38708	0	1380	Line7	1365
27	78.0636	-68.38708	115	1380	Line7	1365
28	78.0636	-68.38708	230	1380	Line7	1365

29	78.06505	-68.37998	-115	1610	Line8	1358
30	78.06505	-68.37998	0	1610	Line8	1358
31	78.06505	-68.37998	115	1610	Line8	1358
32	78.06505	-68.37998	230	1610	Line8	1358
33	78.06651	-68.37261	-115	1840	Line9	1364
34	78.06651	-68.37261	0	1840	Line9	1364
35	78.06651	-68.37261	115	1840	Line9	1364
36	78.06651	-68.37261	230	1840	Line9	1364
37	78.06791	-68.36563	-115	2070	Line10	1365
38	78.06791	-68.36563	0	2070	Line10	1365
39	78.06791	-68.36563	115	2070	Line10	1365
40	78.06791	-68.36563	230	2070	Line10	1365

Table S1. Summary of the active source survey shot locations. For each shot, the latitude and longitude of the first geophone on the line is given. The variable "offset" gives the distance between the source and geophone 1. Negative or positive values indicate that the shot was to the west or east of geophone 1, respectively. The total offset is the distance along the transect, starting in the west.

REFERENCES

Badgeley, J.A., Pettit, E.C., Carr, C.G., Tulaczyk, S., Mikucki, J.A. and Lyons, W.B.: An englacial hydrologic system of brine within a cold glacier: Blood Falls, McMurdo Dry Valleys, Antarctica. J. Glaciol., 63, 387-400, https://doi.org/10.1017/jog.2017.16, 2017.

Burger, H. R., Sheehan, A., & Jones, C. Applied Geophysics: Exploring the Shallow Subsurface, WW Norton, New York, 2006

Cuffey, K. M., & Paterson, W. S. B.: The Physics of Glaciers. Academic Press, 2010

Gundestrup, N. S., & Hansen, B. L.: Bore-hole survey at Dye 3, south Greenland. J. Glaciol., 30, 282–288, 1984

Gusmeroli, A., Pettit, E. C., Kennedy, J. H., & Ritz, C.: The crystal fabric of ice from full-waveform borehole sonic logging. J. Geophys. Res.-EAR, 117, 1–13. https://doi.org/10.1029/2012JF002343, 2012

Kovacs, A., Gow, A. J., & Morey, R. M. The in-situ dielectric constant of polar firn revisited. Cold Reg. Sci. Technol., 23, 245–256. https://doi.org/10.1016/0165-232X(94)00016-Q, 1995

Morlighem, M., Williams, C. N., Rignot, E., An, L., Arndt, J. E., Bamber, J. L., Catania, G., Chauche, N., Dowdeswell, J. A., Dorschel, B., Fenty, I., Hogan, K., Howat, I., Hubbard, A., Jakobsson, M., Jordan, T. M., Kjeldsen, K. K., Millan, R., Mayer, L., Mouginot, J., Noel, B. P. Y., O'Cofaigh, C., Palmer, S., Rysgaard, S., Seroussi, H., Siegert, M. J., Slabon, P., Straneo, F., van den Broeke, M. R., Weinrebe, W., Wood, M., and Zinglersen, K. B.: BedMachine v3: Complete Bed Topography and Ocean Bathymetry Mapping of Greenland From Multibeam Echo Sounding Combined With Mass Conservation, Geophys. Res. Lett., 44, 11051-11061, https://doi.org/10.1002/2017GL074954, 2017.

Muto, A., Anandakrishnan, S., Alley, R. B., Horgan, H. J., Parizek, B. R., Koellner, S., Christianson, K., and Holschuh, N.: Relating bed character and subglacial morphology using seismic data from Thwaites Glacier, West Antarctica, Earth Planet Sc. Lett., 507, 199–206, 2019

Patankar, S.: Numerical heat transfer and fluid flow. Taylor & Francis, 1980

Shreve, R. L.: Movement of Water in Glaciers. Journal of Glaciology, 11, 205–214, https://doi.org/10.3189/S002214300002219X, 1972